THE ASTROPHYSICAL JOURNAL, 393:357–372, 1992 July 1

ORTHO-PARA–HYDROGEN EQUILIBRATION ON JUPITER

BARBARA E. CARLSON, ANDREW A. LACIS, AND WILLIAM B. ROSSOW
Goddard Space Flight Center Institute for Space Studies, 2880 Broadway, New York, NY 10025
Received 1991 June 17; accepted 1992 January 10

ABSTRACT

Voyager IRIS observations have revealed that the Jovian para-hydrogen fraction is not in thermodynamic equilibrium near the NH_3 cloud top. This implies that a vertical gradient exists between the high-temperature equilibrium value of 0.25 at depth and the cloud top values measured by *Voyager*. We use an anisotropic multiple-scattering radiative transfer model to retrieve the height-dependent para-hydrogen profile. While the centers of the $S(0)$ and $S(1)$ hydrogen lines originate near the tropopause (i.e., above the NH_3 cloud top), emission in the wing of the $S(0)$ line originates within the NH_3 cloud layer. The inclusion of spectrally dependent multiple-scattering calculations allows us to use the variation in gaseous absorption strength from the line center to the wing to retrieve the height-dependent para-fraction profile.

We find that a vertical correlation exists between the location of the para-hydrogen gradient and the NH_3 cloud, strongly suggesting that paramagnetic conversion on NH_3 cloud particle surfaces is the dominant equilibration mechanism. Below the NH_3 cloud layer, the para fraction is constant with depth and equal to the high-temperature equilibrium value of 0.25. The degree of cloud-top equilibration appears to depend on the optical depth of the NH_3 cloud layer.

Belt-zone differences exist in the degree of equilibration. Larger, more nearly equilibrated para-fraction values are found in zones. Belt-zone differences in the strength of the para-hydrogen gradient also exist. In belts, the gradient is clearly associated with the location of the NH_3 cloud, and equilibration begins at cloud base, $\approx$0.5–0.55 bar. In zones, "equilibration" does not begin until 0.4 bar, roughly 0.1 bar above the NH_3 cloud base. This difference is most likely a consequence of the advection of low para-fraction values from depth.

Subject headings: atomic processes — planets and satellites: individual (Jupiter)

1. INTRODUCTION

Prior to the *Voyager* IRIS analyses (e.g., Conrath & Gierasch 1983), available observations suggested that equilibration between the ortho ($J = 1, 3, 5, \ldots$) and para ($J = 0, 2, 4, \ldots$) rotational states of hydrogen occurred in the Jovian atmosphere (Smith 1978) with the ratio of the $J = 1$ to the $J = 0$ populations given by Boltzmann statistics. Radiatively the ortho and para states behave as a mixture of two separate gases with the $S(0)$ line at ≈ 360 cm^{-1} formed by transitions between para levels, and the $S(1)$ line at ≈ 590 cm^{-1} originating from transitions between ortho levels. Since opacity within the $S(0)$ and $S(1)$ lines controls the outgoing thermal radiation, the infrared spectra obtained by the *Voyager* spacecraft are sensitive to the value and vertical distribution of para-hydrogen in the Jovian atmosphere. Using the *Voyager* IRIS observations, Conrath & Gierasch (1983) showed that the para-hydrogen fraction near the 0.3 bar level is not in thermodynamic equilibrium, although some degree of equilibration had occurred.

Since transitions for $\Delta J = 1$ are highly forbidden a sample of pure H_2 rapidly cooled from temperatures in excess of 300 K tends to retain its "normal" 3:1 high-temperature para-fraction value of 0.25. Thus, if a para fraction of 0.25 had been observed near the 0.2 bar level, it would have implied that the time scale for the equilibration process is much larger than the time scale for upwelling hydrogen from deeper warmer levels. In contrast, if a para fraction of $\approx$0.35 had been observed, it would have implied that the time scale for equilibration is much faster than the time scale for upwelling hydrogen since this value would be in thermodynamic equilibrium near the NH_3 cloud top where the temperature is $\approx$115 K. The fact that some degree of equilibration, although not complete equilibrium, is observed implies that the time scale for equilibration is comparable to the time scale for upwelling hydrogen. Thus, details of the spatial variation of para fraction may be indicative of characteristics of the mean atmospheric circulation.

Massie & Hunten (1982) reviewed the mechanisms by which hydrogen can equilibrate in the Jovian atmosphere. Based on their analysis of known equilibration processes, they proposed that catalytic reactions between the free-radical surface sites of aerosol particles and hydrogen molecules are responsible for the partial equilibration of the para and ortho rotational levels of molecular hydrogen in the Jovian atmosphere. Photons at wavelengths less than 0.3 μm are required to produce the active surface sites through the production of the NH_2 radical.

In contrast, based on an apparent lack of correlation between cloud indicators (i.e., albedo and 5 μm brightness temperatures), Conrath & Gierasch (1984) concluded that catalysis of ortho-para conversion does not occur on aerosol surfaces. Instead, they proposed H_2-H_2 paramagnetic interactions as the dominant equilibration process at all levels of the atmosphere. Moreover, the slow equilibration rate they inferred has dynamical implications since para-hydrogen conversion greatly increases the efficiency of convection. Finally, Conrath & Gierasch concluded that the global variation of the para fraction could be explained by large-scale upwelling at equatorial latitudes in response to solar heating, advection from lower to higher latitudes, and compensating downward motion in polar regions. In this scenario, upwelling motions carry lower para-fraction parcels up from depth at the equator,

the para fraction steadily increases as parcels are transported toward the poles, and downwelling motions advect more equilibrated para-hydrogen to deeper levels in the polar regions.

The fact that para-hydrogen fractions in excess of the "normal" 0.25 value have been observed, even at the equator, implies that a vertical gradient in the hydrogen para fraction exists. The location of this gradient may provide new insights into the nature of the equilibration process. For example, if catalytic conversion of ortho- to para-hydrogen is occurring on NH_3 cloud particle surfaces, then a correlation should exist between the vertical gradient and the NH_3 cloud location. Moreover, as predicted by Massie & Hunten (1982), a correlation should also exist between the degree of equilibration and the optical depth of the NH_3 cloud due to the particle number density dependence of the rate of the conversion process. In contrast, if the hydrogen para fraction is under dynamic control, then upwelling regions might be expected to have lower para-fraction values, and downwelling regions would be associated with larger para-fraction values. A more detailed and self-consistent analysis of the IRIS data is needed to determine the spatial structure of ortho-para variability.

This investigation is built upon the results of our other investigations (Carlson, Lacis, & Rossow 1992a, b, c) of the nature of cloud structure in the Jovian atmosphere. We have analyzed the *Voyager* IRIS observations over the region $\pm 25°$ latitude, a region that contains the North Tropical Zone (NTrZ), the North Equatorial Belt (NEB), the Equatorial Zone (EqZ), the South Equatorial Belt (SEB), and the South Tropical Zone (STrZ). In this paper, we focus on four extreme dynamic regimes as indicated by the variations in retrieved cloud properties. These regimes correspond to an NEB hot spot spectral ensemble, a cold NEB spectral ensemble, an EqZ spectral ensemble, and an NTrZ spectral ensemble. The NEB hot spots have been selected because these areas are characteristic of intense localized downwelling (mean circulation downwelling combined with a wave downdraft) and contain minimum cloud opacity. The cold NEB ensemble has been selected because these areas are characteristic of *weak* upwelling (mean circulation downwelling combined with a wave updraft). The EqZ ensemble has been selected because the NH_3 cloud in the EqZ is vertically the most extensive, consistent with earlier *Pioneer* results (Coffeen 1974), and suggestive of strong upwelling motions as inferred by Conrath & Gierasch (1984). Further, we have retrieved an NH_3 cloud optical depth of 0.64 from both the EqZ and cold NEB spectral ensembles. The inclusion of these ensembles allows us to separate dynamics and cloud optical depth effects. Finally, the NTrZ subset of the IRIS observations has been included because this region has the largest NH_3 cloud opacity and appears to be associated with a different style of upwelling motions.

In § 2 we briefly describe our radiative transfer model and the method used for our analysis. We emphasize the critical differences between our approach and that used by Conrath & Gierasch (1984). Chief among these differences are our inclusion of spectrally dependent NH_3 cloud extinction, the use of the entire 180–700 cm^{-1} spectral interval to examine the value of the hydrogen para fraction, and the inclusion of a height-dependent para-hydrogen profile. In § 3 we present the results of our analysis, followed by a discussion in § 4.

2. METHOD OF ANALYSIS

The *Voyager* IRIS instrument obtained spectra over the interval 200–2300 cm^{-1} with an apodized spectral resolution of 4.3 cm^{-1} and a noise equivalent radiance of about 7×10^{-9} W cm^{-2} sr^{-1}/cm^{-1} for individual spectra. Extensive sets of Jovian data were acquired by both the *Voyager 1* and *2* flybys (Hanel et al. 1979a, b). An example of a *Voyager* IRIS spectrum is shown in Figure 1. The spectral region of interest for this study lies primarily between 200 and 700 cm^{-1} where the broad $S(0)$ and $S(1)$ hydrogen lines are located, but all results given represent fits to the whole IRIS spectrum. Other sources of opacity within this spectral interval include the rotational lines of NH_3 in the 180–280 cm^{-1} region and NH_3 cloud opacity. Emission features produced by acetylene (C_2H_2) at 729 cm^{-1} and ethane (C_2H_6) at 826 cm^{-1} are apparent in the IRIS observations. These features are stratospheric in origin and are not included in this investigation. In addition, we have not included the absorption due to the hydrogen dimer, which is responsible for the small feature located at 350 cm^{-1}, near the $S(0)$ line center in the *Voyager* IRIS spectrum in Figure 1.

Since the hydrogen ortho and para states behave as a mixture of two separate gases, measurements of these lines provide information on the hydrogen ortho-para ratio. Our procedure for retrieving the para-hydrogen fraction consists of generating synthetic spectra at a spectral resolution of 0.5 cm^{-1}, convolving them with the IRIS instrument function, and comparing them with the *Voyager* IRIS observations. The opacity due to hydrogen is calculated using an algorithm supplied by B. Conrath (1986, personal communication) which uses the absorption coefficients based on the work of Birnbaum & Cohen (1976), but with a temperature dependence based on the work of Bachet et al. (1983) and Dore, Nencini, & Birnbaum (1983). Contributions from H_2-He collisions are included assuming a helium mole fraction of 0.12 (Gautier et al. 1981).

The NH_3 opacity is determined with line-by-line calculations using the GSFC line atlas (cf. Bjoraker, Larson, & Kunde 1986; Kunde et al. 1982). Line shapes for the NH_3 absorption lines are modeled using a Voigt profile (Pierluissi, Vanderwood, & Gomez 1977; Drayson 1975). To account for the sub-Lorentzian behavior of the far wings, we have adopted the common expedient of truncating the Lorentz profile 50 cm^{-1} from the center of each line. We have verified that this choice of line cutoff does not affect our conclusions regarding the cloud properties and the hydrogen para fraction provided that the actual wing contribution extends beyond 10 cm^{-1}. Our spectral integration is standard (Oinas 1983) and similar in many respects to the direct spectral integration techniques developed by Kunde & Maguire (1974) and Scott (1974).

The vertically inhomogeneous atmosphere is subdivided using 15 "homogeneous" layers per decade of pressure spanning the pressure range 0.001–20 bar. Extra layer boundaries are inserted into the model vertical structure coincident with the thermochemically predicted cloud base locations. In the spectral interval of interest, 180–700 cm^{-1}, the radiation originates above 1.5 bar; thus we are only concerned here with the parameterization of the NH_3 cloud layer.

Above the NH_3 condensation level we find that the NH_3 abundance falls off faster than that predicted by saturation. Consistent with the results of previous studies (e.g., Marten et al. 1981; Kunde et al. 1982), we conclude that NH_3 is subsaturated in the above-cloud region. This depeletion is represented by specifying the pressure level above which the depletion occurs and a vapor-to-gas scale height ratio. For the purposes of this study we select this pressure level to be coincident with the location of the NH_3 cloud base.

We evaluate absorption coefficients at the temperatures and

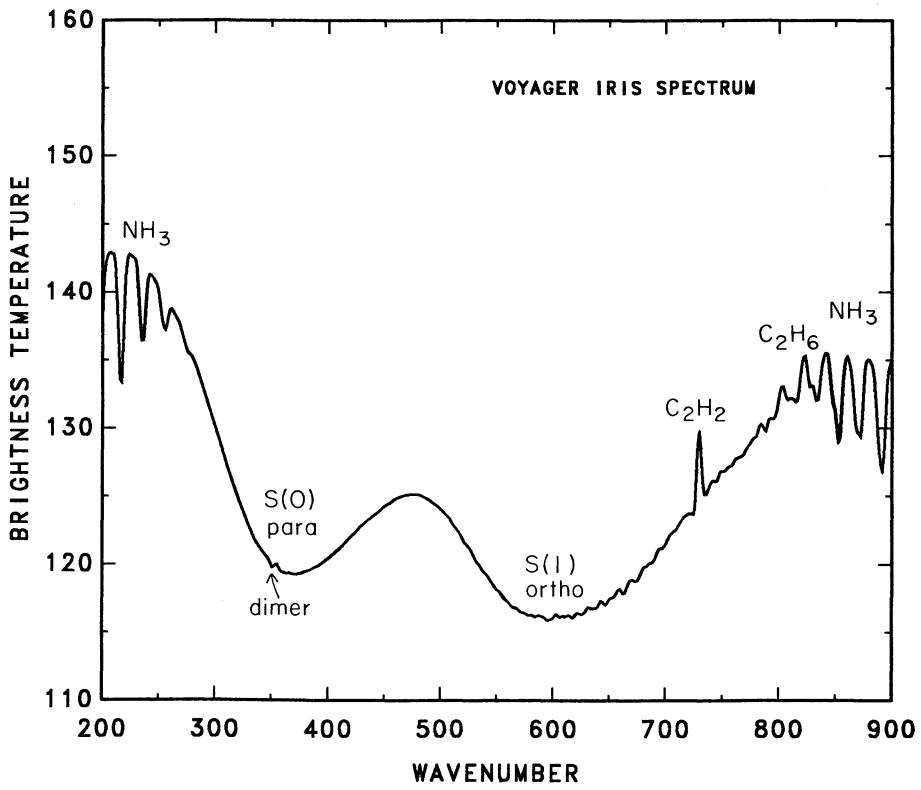

FIG. 1.—Representiative *Voyager* IRIS spectrum. The collision-induced *S*(0) and *S*(1) hydrogen lines result from transitions between para and ortho states, respectively. Absorption by NH_3 dominates the low- and high-frequency ends of this spectral interval. The emission features due to C_2H_2 and C_2H_6 are of stratospheric origin.

pressures corresponding to layer edges and assume that the absorption coefficients vary linearly between the upper and lower layer boundaries. In the case of hydrogen, the pressure-squared dependence of the absorption coefficient is explicitly included by means of analytic weighting factors that accurately account for the pressure-temperature layering structure used in the model.

For numerical efficiency and more accurate modeling of the atmospheric temperature profile, we represent the intralayer temperature gradient as being linear in Planck function. We use the doubling equations to calculate the effects of multiple scattering on the reflection, transmission, and thermal emission for homogeneous layers. The adding equations are used to obtain the reflection, transmission, and emission for composite (inhomogeneous) layers. The details of the thermal doubling and adding method are given in Carlson et al. (1992a, henceforth CLR92a).

For diagonostic purposes, we calculate a normalized cumulative contribution function to determine the fractional contribution of each model layer to the total outgoing radiation at each wavelength. Since the normalized contribution function includes the effects of atmospheric temperature on Planck emission, it more accurately depicts the level of peak emission in the atmosphere than the more traditional criterion of unit optical depth.

The spectral dependence of cloud particle extinction is obtained from Mie calculations, which are performed assuming a gamma size distribution (eq. [2.56] of Hansen & Travis 1974) for a variety of values of effective particle radius a and effective variance b. The optical properties for NH_3 ice (Martonchik, Orton, & Appleby 1984) are used to determine the scattering and extinction efficiency factors, Q_{scat} and Q_{ext}, respectively. The vertical distribution of cloud opacity (and vertical extent of the cloud) is represented by a particle-to-gas scale height ratio.

Cloud optical depth is expressed as τ_{ref}, an extinction optical depth referenced at visible wavelengths, $\lambda = 0.5$ μm, where the Mie calculated efficiency factors are normalized to unity. At wavelengths of interest, the monochromatic cloud optical depth is then given by the product of τ_{ref} and the value of Q_{ext} at that particular wavelength. Within any atmospheric layer, the monochromatic single-scattering albedo is the ratio of the total scattering optical depth ($\tau_{ref}\,\tilde{\omega}_0\,Q_{ext}$) to the total extinction optical depth ($\tau_{ref}\,Q_{ext} + \tau_{gas}$), and is therefore strongly wavelength and altitude dependent.

Retrieval of the NH_3 cloud properties is discussed in detail by CLR92a. Basically, to reproduce the observed spectral dependence of cloud extinction, most of the NH_3 cloud particles must be large. Our best fit to the IRIS observations is obtained with a bimodal distribution of cloud particles with effective radii of 3 and 100 μm. The bulk of the cloud mass and opacity is provided by the large particle mode. The large particles are required to provide sufficient extinction in the 50 μm (180–300 cm^{-1}) region of the spectrum, where small particles are much too inefficient, without violating constraints from the 5 μm portion of the spectrum. Smaller NH_3 particles, with sizes more comparable to the wavelengths of observation, are required to reproduce the shape of the continuum, primarily between 200–300 cm^{-1}, but also between 440 and 520 cm^{-1}.

The range of effects that NH_3 cloud extinction has on the

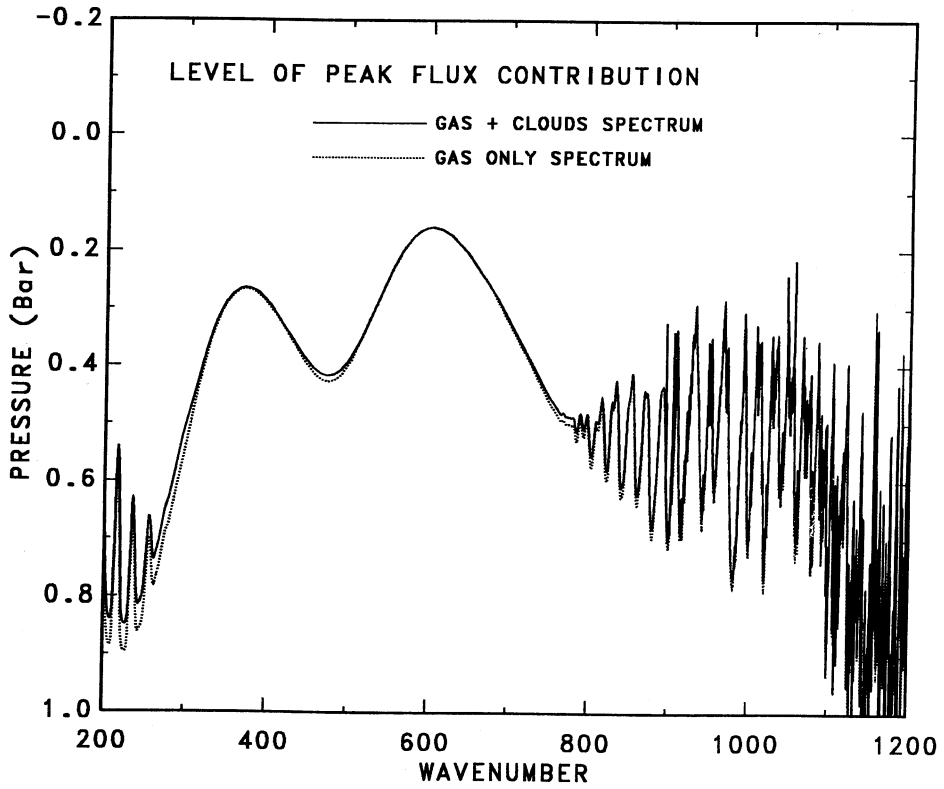

FIG. 2*a*

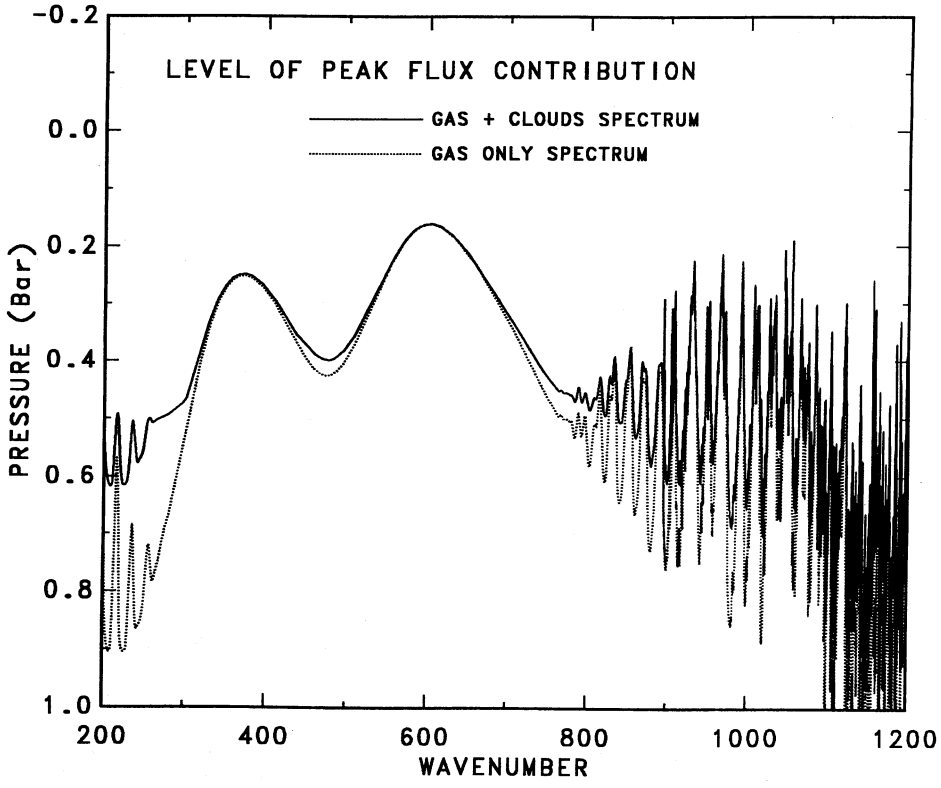

FIG. 2*b*

FIG. 2.—Comparison of the location of the peak emission level calculated with (*solid line*) and without (*dotted line*) the inclusion of cloud opacity using our NEB hot spot model (*a*) and our NTrZ model (*b*) for the far-infrared (200–1200 cm^{-1}) region.

spectrum can be seen from a comparison of the peak emission level calculated with and without the inclusion of NH_3 cloud opacity using our NEB hot spot model (Fig. 2*a*) and using our NTrZ model (Fig. 2*b*), representing the lowest and highest NH_3 cloud optical depths found. Radiation in the 200–700 cm^{-1} region of the spectrum originates from pressures less that 1 bar. Cloud extinction is important in the 200–330 and the 420–520 cm^{-1} regions. The effect that cloud opacity has on the spectrum obviously depends on the optical depth of the cloud. In the NTrZ where the NH_3 cloud has an optical depth near unity the cloud has a larger effect on the location of the peak emission level as evidenced by the larger difference between the peak emission levels calculated with and without the cloud. Further, since the temperature profile in the NTrZ is roughly 2° C colder than that in the NEB, consistent with the results of Hanel et al. (1979a), the effect that differences in the thermal structure have on the spectrum can be seen by comparing the two gas-only cases. In particular, variations in the temperature profile alter the shape of the hydrogen absorption features but do not significantly change the depth of the absorption features. Finally, redundant cloud information is contained in the 700–1200 cm^{-1} region of the spectrum. By analyzing the whole spectrum we are better able to separate temperature, cloud, and para-fraction effects than previous investigations which focused only on the information content of the IRIS measurements at several discrete wavelengths.

In order to be able to retrieve the hydrogen para fraction, its variation must produce detectable variations in the observed spectrum. Figure 3 shows the overall magnitude of the spectral response to variations in para fraction for vertically uniform distributions with $f_p = 0.25$ (solid line) and $f_p = 0.35$ (dashed line). The difference between the two synthetic spectra, plotted in the lower portion of the figure, is substantially larger than the standard deviation of the individual NEB hot spot spectra (dotted lines). Thus the IRIS observations can be used to constrain the hydrogen para fraction in the Jovian atmosphere. Further, based on the location of the peak emission level, shown in the previous figure, we see that the IRIS measurements provide information on the para-fraction *profile* over a pressure range of 0.1–0.9 bar.

The spectral region near 520 cm^{-1} is insensitive to the hydrogen para fraction because, for ortho and para hydrogen, the absorption coefficients are essentially equal at this wavenumber. Also, as noted by Conrath & Gierasch (1984), the $S(1)$ line center near 600 cm^{-1} is relatively insensitive to f_p because its unit optical depth occurs near the tropopause where the lapse rate is small; hence the emitted radiances at these two wavelengths are not strongly dependent on changes in the vertical distribution of atmospheric opacity. This region of the spectrum is also insensitive to the NH_3 cloud structure since the $S(1)$ line forms well above the NH_3 cloud top. For these reasons, we use the 520–700 cm^{-1} region of the spectrum to constrain the temperature structure in the upper troposphere. Additional thermal structure information is obtained from the 900–1200 cm^{-1} region. The warmest synthetic spectra result from a "normal" para fraction since this imposes less absorption in the $S(0)$ line region than the "equilibrium" value of 0.35.

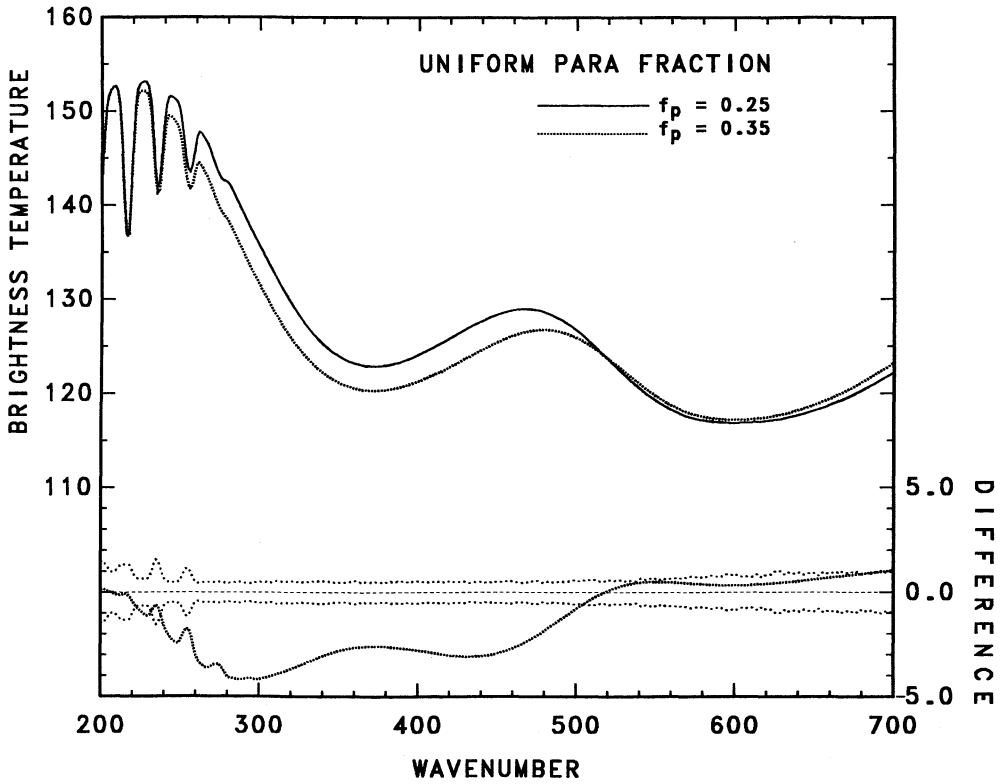

FIG. 3.—Comparison of synthetic spectra calculated with a uniform para fraction of 0.25 (*solid line*) and 0.35 (*dotted line*). The standard deviation of the individual spectra comprising the IRIS NEB hot spot spectral ensemble is shown (*heavy dotted line*) in the lower portion of the figure along with the difference between the two synthetic spectra. Since the difference between the synthetic spectra is much larger than the standard deviation of the IRIS observations, the IRIS observations can be used to constrain the value of the para fraction in the Jovian atmosphere. Note that the region between 240 and 520 cm^{-1} is most sensitive to the value of the hydrogen para fraction.

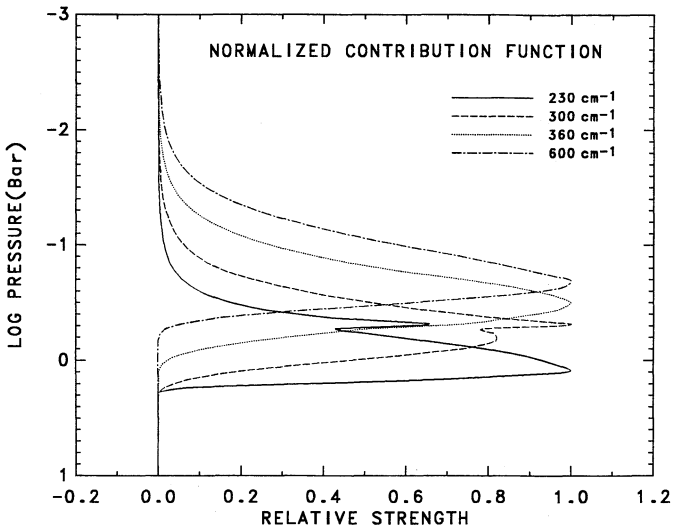

FIG. 4a

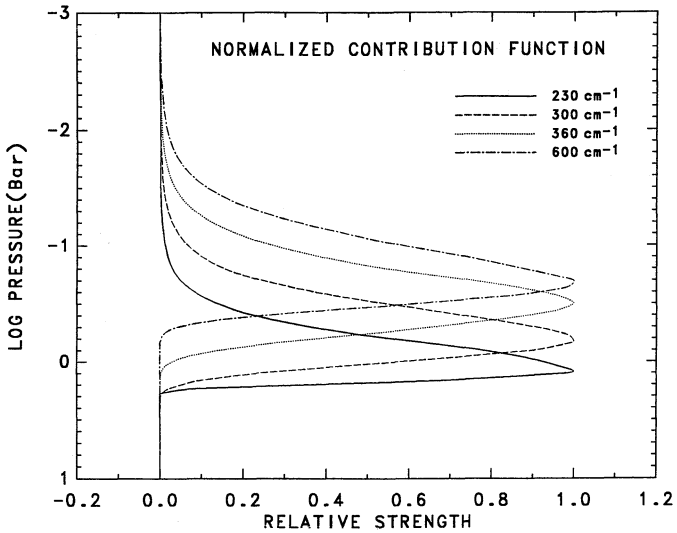

FIG. 4b

FIG. 4.—Comparison of the normalized contribution functions calculated at 230 (*solid line*), 300 (*dashed line*), 360 (*dotted line*), and 600 cm^{-1} (*dash-dot line*) with (*a*) and without (*b*) the inclusion of NH_3 cloud opacity. The lack of any change in the shape of the normalized contribution function between (*a*) and (*b*) at 360 and 600 cm^{-1}, corresponding to the centers of the *S*(0) and *S*(1) hydrogen lines, respectively, illustrates that radiation at these wavelengths is insensitive to the presence of the NH_3 cloud layer. Radiation at 230 cm^{-1} and in the wing of the *S*(0) hydrogen line at 300 cm^{-1} contains a significant contribution from the NH_3 cloud as evidenced by the double-peaked structure of the normalized contribution function.

The degree to which outgoing radiation in the 200–600 cm^{-1} interval is affected by NH_3 cloud opacity depends on the location of the peak emission level relative to cloud base. Figure 4 compares normalized contribution functions calculated using our NEB hot spot model, with (Fig. 4*a*) and without (Fig. 4*b*) the inclusion of NH_3 opacity for the wavenumbers of 360 and 600 cm^{-1}, which correspond to the centers of the *S*(0) and *S*(1) hydrogen lines, respectively. At these wavelengths, the contribution functions show no change between Figures 4*a* and 4*b*, confirming that radiation at the *S*(0) and *S*(1) line centers is insensitive to the NH_3 cloud. However, at 230 cm^{-1} and in the wing of the *S*(0) hydrogen line at 300 cm^{-1}, the emission originates from larger pressures and contains a significant contribution from the NH_3 cloud as evidenced by the double-peaked structure of the contribution functions in Figure 4*a* relative to the single-peaked (gas only) contribution functions in Figure 4*b*. Therefore, it is essential that NH_3 cloud extinction be included in the determination of the hydrogen para fraction.

To test the notion that the para fraction is related to the strength and/or sign of the local dynamics (as proposed by Conrath & Gierasch 1984), we use four subsets of IRIS observations corresponding to extreme dynamical regimes. One subset corresponds to hot spots within the Jovian NEB which are identified by imposing the same selection criteria used by Kunde et al. (1982). This subset of IRIS observations has fields of view smaller than 5° in latitude, limiting the observations to within ± 1 day of closest approach; the center of the IRIS field of view (FOV) must fall between 7° and 13° N latitude. The average 45 μm (defined to be 226 $\pm$ 2 cm^{-1}) brightness temperature must be $\geq$149 K, the average 5 μm (defined to be the average over the interval 2050 $\pm$ 100 cm^{-1}) brightness temperature must be $\geq$250 K, and the emission angle must be less than 30° corresponding to μ (cosine of the emission angle) greater than 0.866. These regions have minimum cloud opacity and appear to correspond to areas of enhanced downwelling with respect to the whole NEB which appears to be a general region of downwelling (CLR92a). We have also included a cold NEB spectral ensemble. This region, in addition to satisfying the FOV, latitude, and emission angle selection criteria listed above, is characterized by 45 μm brightness temperatures between 140 and 149 K and 5 μm brightness temperatures between 200 and 230 K.

In contrast, the NTrZ, which appears to be a homogeneous region of upwelling, contains some of the coldest spectra at 5 and 45 μm. For the purposes of this investigation we have selected a subset of the coldest NTrZ spectra. We apply the same emission angle and field-of-view selection criteria, but now the center of the IRIS field of view must be between 17° and 23° N latitude. The average 45 μm brightness temperature must be less than 146 K, and the average 5 μm brightness temperature less than 205 K.

For our EqZ spectral ensemble we again employ the same emission angle and field-of-view selection criteria, but now the center of the IRIS field of view must lie between 3° S and 3° N latitude. The average 45 μm brightness temperature must be between 144 and 149 K, and the average 5 μm brightness temperature must be less than 205 K. Figure 5 compares the average IRIS spectra corresponding to the NEB hot spot, EqZ, and NTrZ subsets. The NEB hot spot spectrum consists of an average of 52 individual IRIS spectra, the cold NEB ensemble (not shown) contains 76 spectra, while the EqZ subset contains 32 spectra and the NTrZ spectrum is an average of 74 individual IRIS spectra.

Based on our previous investigation into the nature of the Jovian cloud structure and belt-zone differences (CLR92a), we find the NEB hot spot observations are best fitted with an NH_3 cloud optical depth of 0.27, referenced at $\lambda = 0.5$ μm, with $\tau = 0.19$ provided by the large particles. Within NEB hot spots, NH_3 cloud opacity is distributed according to a particle-to-gas scale height ratio H_p/H_g of 0.15 above cloud base which is located near 0.5 bar. In the colder NEB ensemble, the NH_3

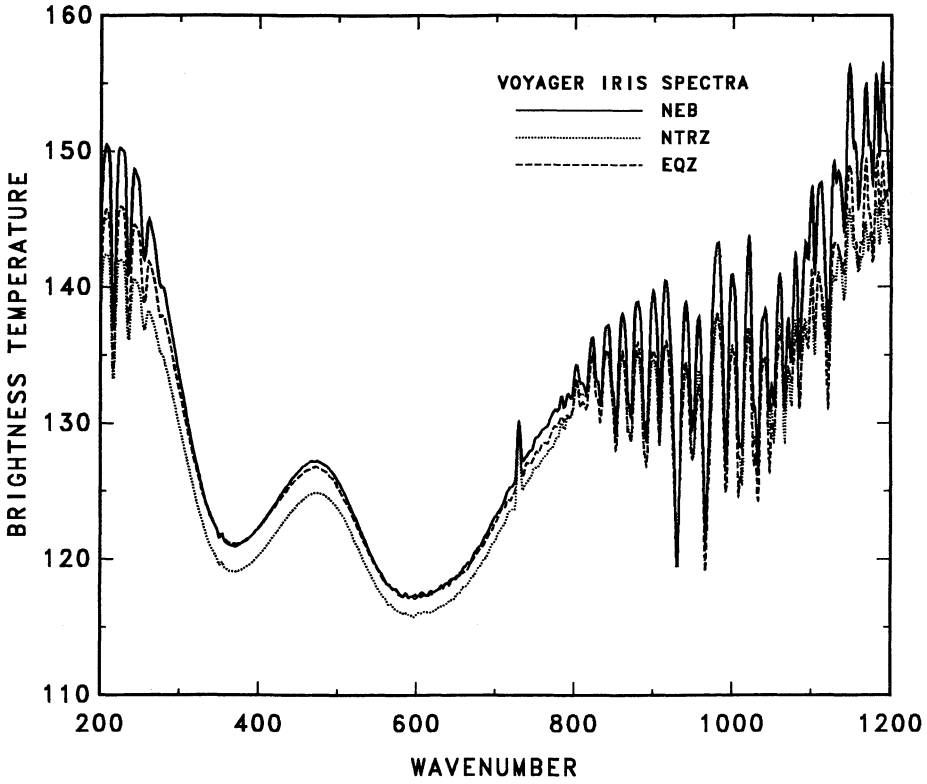

FIG. 5.—Comparison of the average IRIS spectra corresponding to each of our spectral ensembles. The higher brightness temperatures observed in the NEB hot spots (*dotted line*) are indicative of an optically thinner NH_3 cloud layer in these regions. The EqZ spectral ensemble (*dashed line*) is similar to the NEB spectral ensemble in the regions of the $S(0)$ and $S(1)$ hydrogen lines; however, larger differences are seen at the low- and high-frequency ends of this spectral interval due to differences in the opacity of the NH_3 cloud. The NTrZ spectral ensemble (*solid line*) is unique in that the region is much colder than the other spectral ensembles as evidenced by the nearly constant offset between the spectra.

cloud has a larger optical depth. In this case, the total optical depth is 0.64 with $\tau = 0.52$ provided by the large particles distributed according to a particle-to-gas scale height ratio of 0.1. The small particles are distributed following $H_p/H_g = 0.15$. In addition, the NH_3 cloud base is shifted to higher pressure (0.57 bar) due to small variations in the NH_3 vapor and temperature profiles. This cloud opacity distribution is more complex than that found in the hotter NEB ensembles and in many respects similar to the NH_3 cloud structure present in zones.

The NH_3 cloud in the EqZ has a similar, although more complicated, two-part structure with an optical depth of 0.64; however, the bulk of the cloud mass is distributed with a particle-to-gas scale height ratio of 0.20, with a small fraction of the cloud opacity, $\tau = 0.12$, concentrated near the cloud base at 0.52 bar with a particle-to-gas scale height ratio of 0.05. In contrast, in the NTrZ most of the cloud mass is concentrated near the base of the NH_3 cloud which forms near 0.5 bar. The total optical depth of the NH_3 cloud is 0.97, with $\tau = 0.92$ provided by the large particles distributed according to a particle-to-gas scale height ratio of 0.03. A small amount of opacity, $\tau = 0.07$, is distributed vertically according to a particle-to-gas scale height ratio of 0.2.

If we refer to the level at which $\tau = 10^{-3}$ as "cloud top," then cloud tops in the NEB hot spots occur at about 0.22 bar, while in the colder NEB ensemble the cloud top is located near 0.19 bar. The cloud top in the EqZ occurs near 0.10 bar, while the cloud top occurs at approximately 0.16 bar in the NTrZ. These differences in the vertical distribution of cloud opacity are consistent with the differences in the dynamic regime between these four regions (Carlson et al. 1992b). These cloud structures are typical of the range of structures that have been observed in cirrus clouds on Earth (cf. Sassen et al. 1990). Thus these four regions form a unique set of observations with which to examine spatial variations in the value of the para-hydrogen fraction and the possible influence that dynamics and/or NH_3 cloud opacity have on ortho-para equilibration.

3. RESULTS

NH_3 cloud opacity alters emission in the wing of the $S(0)$ hydrogen line, even in NEB hot spots which have the least NH_3 cloud opacity ($\tau = 0.27$) of any location on Jupiter (Fig. 2*a*). Figure 6 shows synthetic spectra calculated for uniform para fractions of 0.25, 0.27, 0.30, and 0.35 with (Fig. 6*a*) and without (Fig. 6*b*) NH_3 cloud opacity compared to the average NEB hot spot IRIS spectrum. Differences between the observed and synthetic spectra are plotted in the lower portions of Figures 6*a* and 6*b* along with the standard deviation of the individual spectra comprising the hot spot ensemble. None of these synthetic spectra, calculated with a constant para-fraction profile, provide an acceptable fit to the average IRIS spectrum. In all cases the difference between the synthetic and observed spectra is larger than the standard deviation of the individual IRIS spectra comprising the average ensemble.

NH_3 cloud opacity is clearly required in the 200–260 cm^{-1} region of the spectrum to reduce the gas-only model contin-

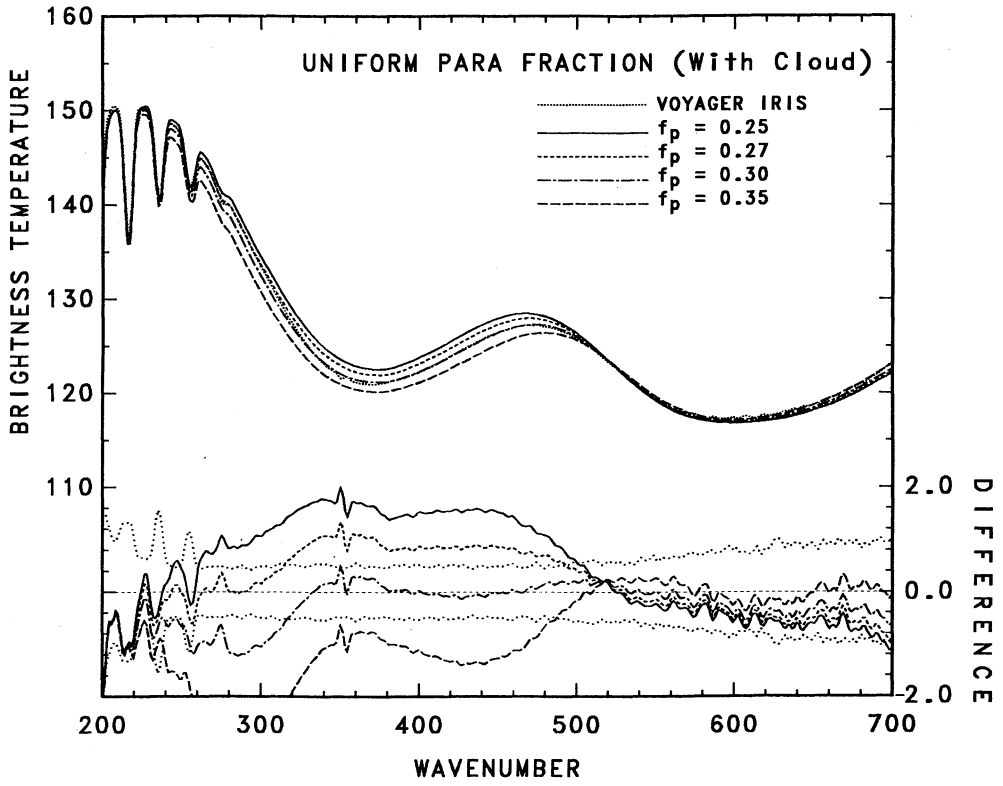

FIG. 6*a*

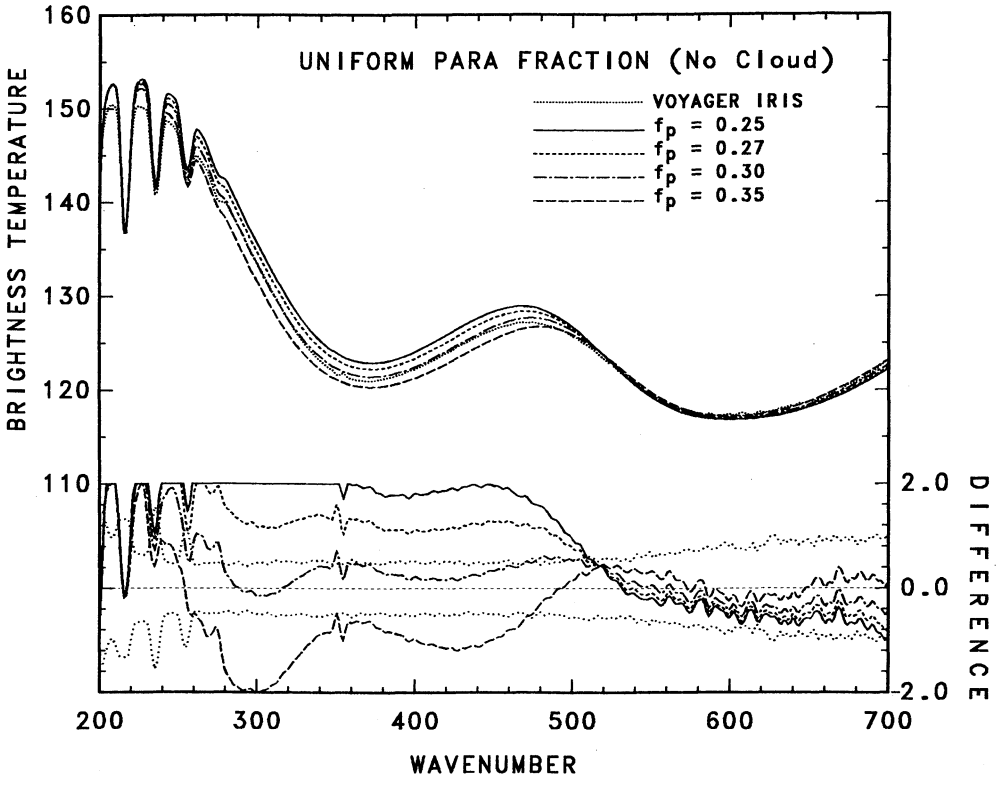

FIG. 6*b*

FIG. 6.—The effect that NH_3 cloud opacity has on the retrieval of the hydrogen para fraction is illustrated through the comparison of synthetic spectra calculated for uniform para fractions of 0.25 (*solid line*), 0.27 (*short dashed line*), 0.30 (*dash-dot line*), and 0.35 (*long dashed line*) with (*a*) and without (*b*) the inclusion of NH_3 cloud opacity. The average IRIS hot spot spectrum (*dotted line*) is shown for comparison. Difference spectra are plotted in the lower portion of the figure along with the standard deviation of the IRIS spectral ensemble.

uum to match that of the IRIS observations. In the absence of NH_3 cloud opacity (Fig. 6*b*), a para fraction of 0.30 appears to provide the closest fit to the IRIS observations. However, once spectrally dependent cloud opacity is included, as in Figure 6*a*, a more complicated f_p profile is required. Since the radiation in the centers of the $S(0)$ and $S(1)$ hydrogen lines comes from levels above the NH_3 cloud and is relatively insensitive to its presence, an f_p of 0.30 still provides the closest fit to the IRIS observations in the hydrogen line centers. However, the NH_3 cloud contributes substantial absorption in the wing of the $S(0)$ line near 300 cm^{-1}. Here, a para fraction of 0.27 provides the best fit to the IRIS observations. Based on this shift in para fraction with the location of the peak emission level from the $S(0)$ line center to the wing, as illustrated by the normalized contribution function in Figure 4, we conclude that a height-dependent para-fraction profile is required to fit the IRIS observations. Note, however, that had we restricted this investigation to three discrete wavelengths, 330, 520, and 600 cm^{-1}, as did Conrath & Gierasch (1984), then we would have erroneously concluded that a height-independent para-hydrogen profile with a para-fraction of 0.3 provides an acceptable fit to the IRIS measurements. Thus, a key difference between our investigation and the previous investigations is that we consider the full 200–700 cm^{-1} region and require that our best-fit model reproduce the IRIS observations to within the standard deviation of the individual IRIS spectra comprising the ensemble throughout this spectral interval.

The vertical distribution of f_p can be inferred from the differential absorption strength from line-center to line-edge of the $S(0)$ line as discussed above. This approach was also used by Gierasch, Conrath, & Magalhães (1986) but with NH_3 cloud effects and height dependence of the para-hydrogen profile neglected. While the depth of the $S(0)$ hydrogen line is primarily controlled by f_p at higher levels, the shape of the wing is controlled by the variation of f_p with altitude. Figure 7 shows a schematic representation of the height-dependent para-fraction profile that provided the best fit to the NEB hot spot spectral ensemble. The height-dependent profile starts with the high-temperature equilibrium value of $f_p = 0.25$ at depth. In this simplified form, the specification of the inflection points P_L and P_U, defines the gradient of the hydrogen para fraction between the deep atmosphere "normal" value below P_L and the more equilibrated cloud top value above the pressure level P_U.

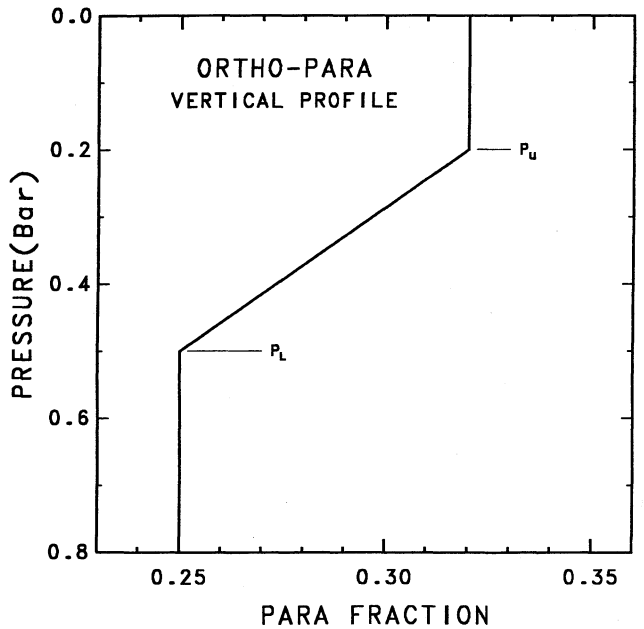

FIG. 7.—Schematic representation of our best-fit height-dependent para-fraction profile to the NEB hot spot spectral ensemble. The inflection points P_L and P_U define the gradient of the para-fraction between the deep atmosphere "normal" value below P_L and the equilibrated cloud top value above P_U.

Figure 8 compares the average hot spot spectrum (dotted line) and our best-fit synthetic spectrum (solid line) calculated with the height-dependent para-fraction profile shown in Figure 7. The difference between the synthetic and observed spectra is plotted in the lower portion of the figure (solid line) along with the standard deviation of the IRIS spectra (dotted line). The relatively poorer fit near 200 cm^{-1} arises in part from uncertainties in the treatment of the line shapes for the far-infrared rotational lines of NH_3 and from increased noise in the IRIS observations near this extreme in its spectral range. Absorption by the H_2 dimer, evident in the difference spectrum near 350 cm^{-1}, has been neglected for these calculations.

The standard deviation of the IRIS spectra, shown in Figure 8, is much larger than the instrument noise level and represents real variations of conditions within different hot spots. We have obtained a single, average result for these locations, but illustrate in Figure 9 the range of variations in the vertical profile of f_p that are allowed within the standard deviation of the spectra. Figure 9*a* shows that by shifting P_L from 0.5 bar to higher pressure, the column amount of para-hydrogen is increased and thus results in a colder spectrum, while decreasing P_L results in a warmer spectrum. Similarly, shifting P_U from 0.2 bar to higher pressure (Fig. 9*b*) results in a colder spectrum, while decreasing P_U results in a warmer spectrum. Likewise, increasing the value of the cloud top (equilibrated) para fraction from 0.32 produces a colder spectrum (Fig. 9*c*). (Note that the IRIS spectra are sensitive to the value of f_p up to about 0.1 bar). Thus, there is a range of compensating adjustments to the f_p gradient parameters that can explain the variation of the hot spot spectra. Our best fit to the average NEB hot spot IRIS spectrum has $P_L = 0.50 \pm 0.1$ bar, $P_U = 0.2 \pm 0.1$ bar, $f_p = 0.32 \pm 0.01$ for the cloud top (equilibrated) para fraction and $f_p = 0.25 \pm 0.01$ at depth. Thus in NEB hot spots, the location of the para-hydrogen gradient appears to be coincident with the location of the NH_3 cloud.

Hot spots represent an extreme within the NEB. Figure 10 shows a comparison of our best-fit synthetic spectrum (solid line) to the cold NEB ensemble spectrum (dotted line). The colder 45 μm brightness temperatures, as shown in the 200 to 600 cm^{-1} region of the spectrum, are indicative of an optically thicker NH_3 cloud ($\tau = 0.64$) in this spectral ensemble relative to that in the NEB hot spots. While the para-fraction profile retrieved for hot spots provides a technically acceptable fit (i.e., the difference between the synthetic and observed spectra falls within the standard deviation of the individual spectra), a slightly more equilibrated para-fraction profile improves the quality of the fit. Our best-fit para fraction profile for this colder spectral ensemble has $P_L = 0.55$ bar, $P_U = 0.10$ bar, $f_p = 0.33$ for the cloud top para-fraction, and $f_p = 0.25$ at depth, although values in the range of 0.25–0.26 are acceptable.

The downward shift in P_L toward higher pressure correlates with a shift in the NH_3 cloud base from 0.52 bar in hot spots to 0.57 bar in this colder spectral ensemble; however, the upward shift in P_U does not correspond to any significant change of

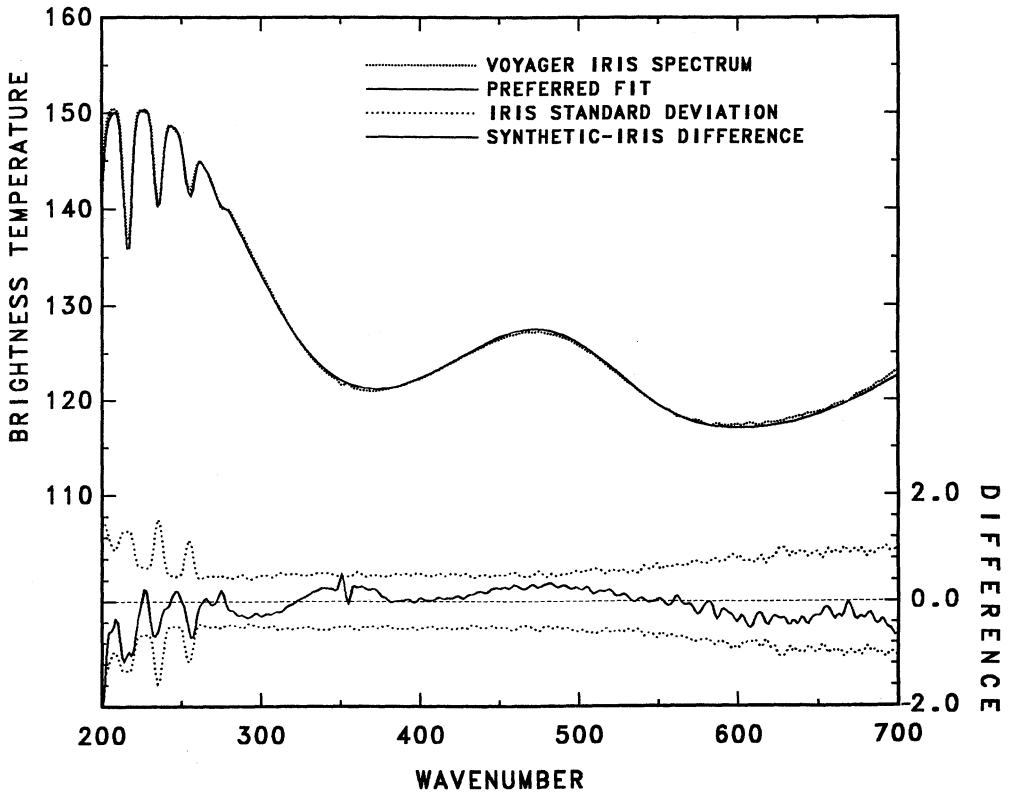

FIG. 8.—Comparison of our best-fit synthetic spectrum calculated with the height-dependent para-fraction profile shown schematically in Fig. 7 (*solid line*) and the average IRIS NEB hot spot spectrum (*dotted line*). The difference between the observed and synthetic spectra is shown in the lower portion of the figure (*solid line*) along with the standard deviation of the individual IRIS spectra comprising the ensemble (*dotted lines*). The difference is less than the standard deviation of the IRIS spectra at all wavelengths.

cloud top. The increased para fraction near the NH_3 cloud top correlates with the larger NH_3 cloud optical depth in this region relative to that found in NEB hot spots.

To further test these associations of para-fraction profile and cloud structure, we analyzed the zone spectral ensembles. Figure 11 shows our best fit to the cold Equatorial Zone spectral ensemble. The value of the "equilibrated" para fraction is 0.33 at 0.2 bar. Although NH_3 cloud opacity extends to lower pressure (about 0.12 bar), the bulk of the cloud mass is located below the 0.2 bar level. The NH_3 cloud base forms near 0.52 bar, but the location of P_L is shifted to 0.4 bar. This shift in the location of the inflection point P_L appears to be real and may be indicative of stronger dynamical upwelling in the EqZ.

In our best fit to the NTrZ spectral ensemble, shown in Figure 12, the para fraction increases from 0.25 at 0.4 bar to 0.35 at 0.2 bar. Although the NH_3 cloud top extends to just above the 0.2 bar level, most of the NH_3 cloud mass is located below the 0.3 bar level. Again, the location of P_L at 0.4 bar is not coincident with the NH_3 cloud base, which is located at 0.5 bar. The cold NTrZ spectral ensemble has the most equilibrated value of the hydrogen para fraction near cloud top.

We have also obtained results for the SEB (latitude = $-7°$ to $-13°$) and the STrZ (latitude = $-17°$ to $-23°$), excluding longitudes containing the Great Red Spot. The results for these regions are similar to those from corresponding regions in the northern hemisphere. We have found that there is a consistent belt-zone difference in the location of the para-hydrogen gradient. The "zone" profile exhibits more equilibrated values of f_p above 0.2 bar, but the transition from the deep f_p value of 0.25 occurs over a shallower layer beginning near 0.4 bar, above the base of the NH_3 cloud. The "belt" profile exhibits less equilibrated values of f_p above the 0.2 bar level with a more gradual transition over a deeper layer beginning near 0.52 bar, coincident with the base of the NH_3 cloud.

4. DISCUSSION

In all cases, we find the location of the para-hydrogen gradient to be confined *within* the NH_3 cloud. Moreover, horizontal variations of para fraction are correlated with horizontal variations of NH_3 cloud optical thickness. This strong spatial association of the para fraction and the NH_3 cloud mass suggests catalytic reactions on NH_3 cloud particles to be the primary equilibration mechanism in the upper troposphere as predicted by Massie & Hunten (1982). Further strengthening this conclusion and consistent with the predictions of Massie & Hunten, we find that above the NH_3 cloud, the ortho-para ratio appears to retain its characteristic "cloud top" value as illustrated in Figure 7. However, since variations in the structure of a condensate cloud are likely to correlate with variations in dynamics, variations in the strength of the vertical mixing are also required to explain some of the spatial correlations that we observe.

For their calculations, Massie & Hunten (1982) used a simple one-dimensional aeronomical model which contained the competing influences of mixing (vertical eddy diffusion) and

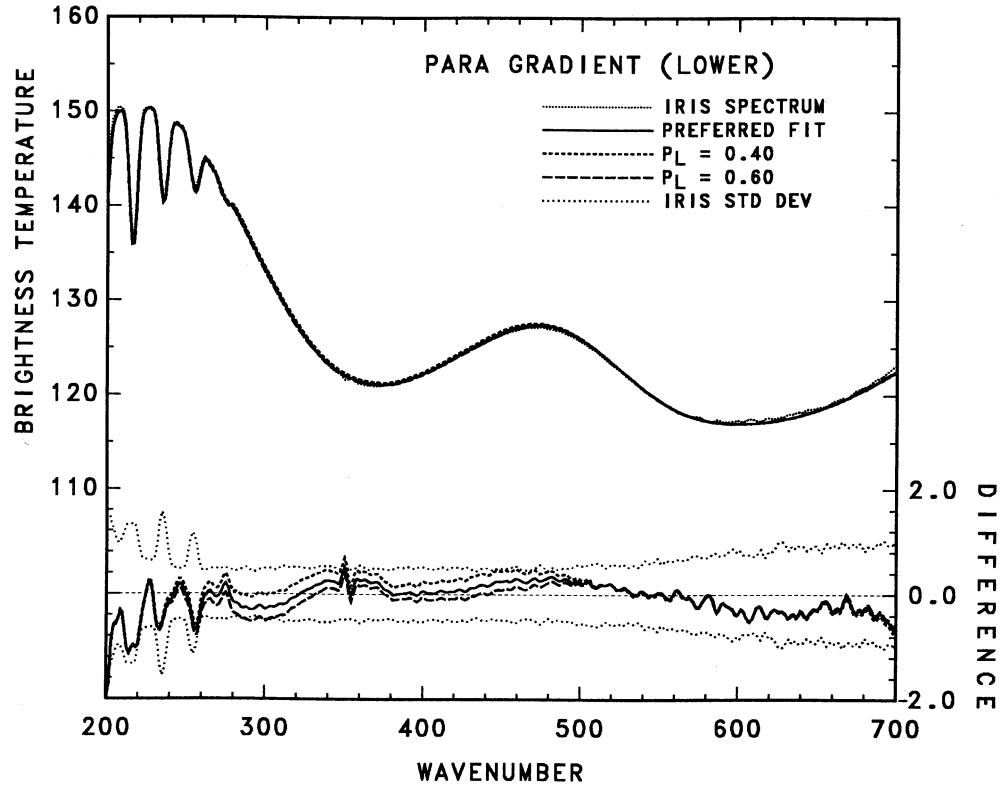

FIG. 9*a*

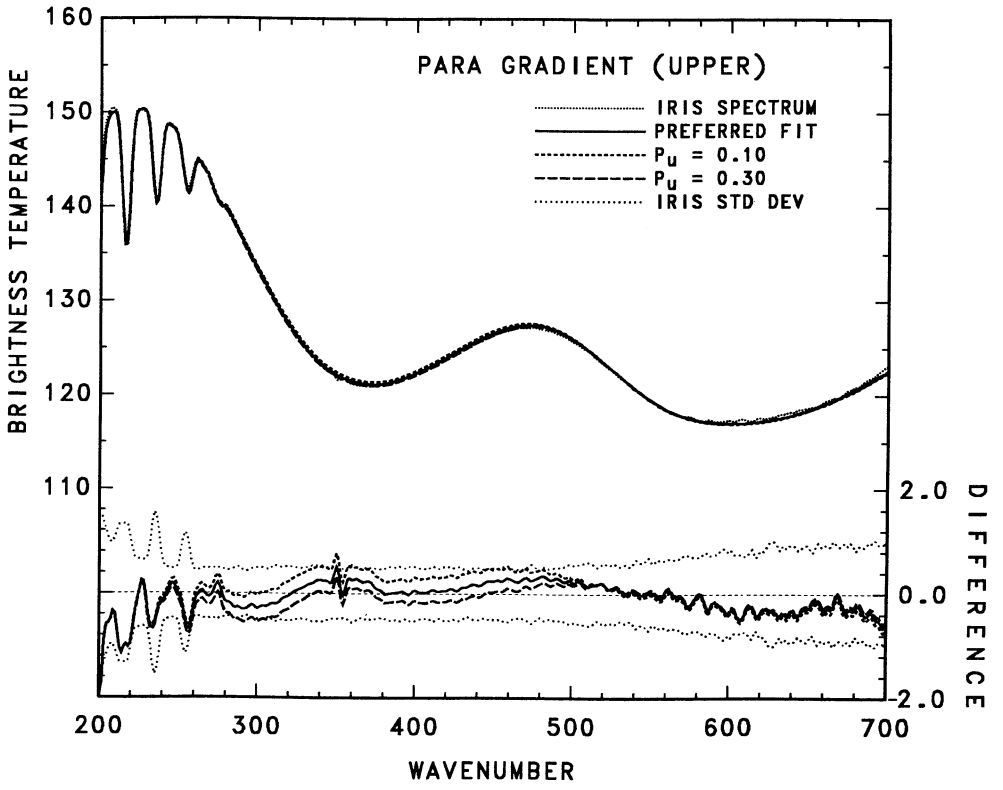

FIG. 9*b*

FIG. 9.—Illustration of the sensitivity of the synthetic spectrum to variations in the parameters controlling the height-dependent para-fraction profile. (*a*) Comparison of synthetic spectra calculated using our best fit para-fraction profile (*solid line*) with spectra calculated using $P_L = 0.4$ bar (*short dashes*) and $P_L = 0.6$ bar (*long dashes*) to the average NEB hot spot spectrum. The difference between the synthetic and observed spectra is plotted in the lower portion of the figure along with the standard deviation of the individual IRIS spectra comprising the average spectral ensemble. Note that if $P_L = 0.6$ bar, the synthetic spectrum is no longer able to reproduce the IRIS observations to within the standard deviation of the observations near 300 cm^{-1}; similarly, $P_L = 0.4$ bar runs into difficulty near 350 and 460 cm^{-1}. A similar response in the spectral sensitivity is obtained for variations in P_U shown in (*b*) and f_p shown in (*c*).

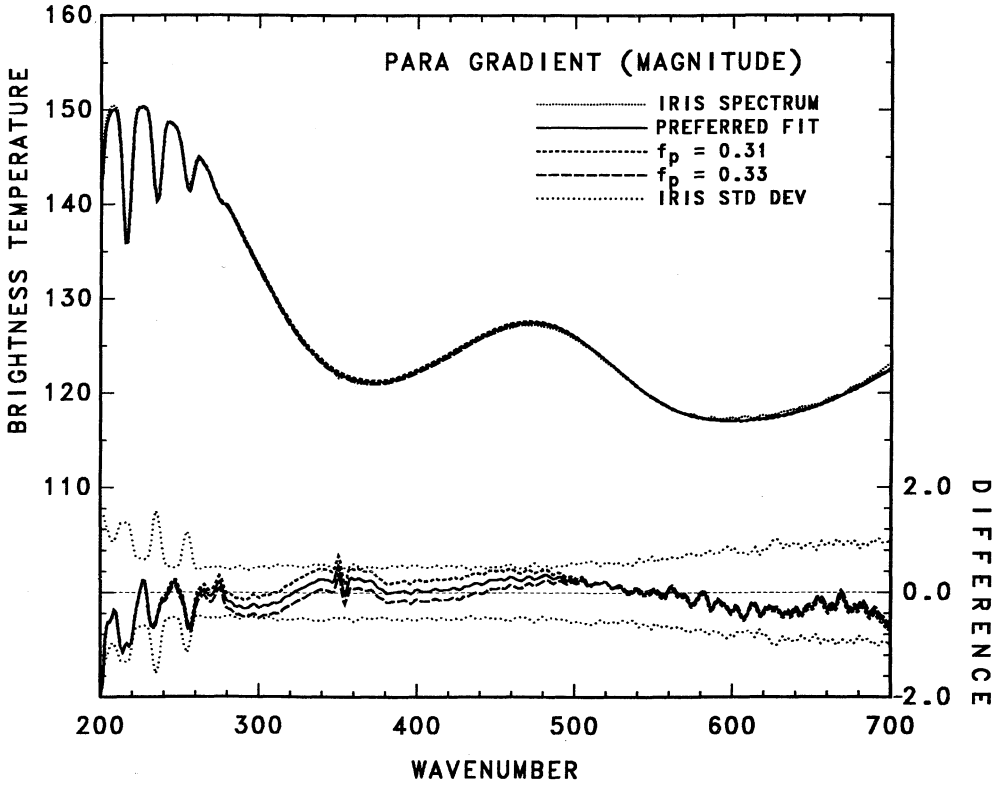

FIG. 9c

ortho-para conversion. With this model, they concluded that catalytic reactions upon aerosol particles can equilibrate ortho- and para-hydrogen provided that the conversion rate C is $\approx 10^{10}$ cm^3 s^{-1}, and that the NH_3 cloud particles are located in gas that is being mixed by an effective eddy coefficient of $K = 10^4$ cm^2 s^{-1}. The important point here is that the degree of equilibration scales according to the ratio C/K.

We can rescale the Massie & Hunten (1982) calculations using our retrieved NH_3 cloud properties. For their calculations Massie & Hunten assumed 1 μm radius NH_3 cloud particles distributed over a 5 km layer with a visible optical depth of 3. In contrast, we have found 100 μm radius cloud particles (although the upper levels of the NTrZ/STrZ are dominated by 3 μm particles) that are distributed over a 10–20 km layer with visible optical depths in the range of 0.27–0.97.

Massie & Hunten (1982) concluded that the effective eddy coefficient must be of order 10^4 cm^2 s^{-1} in order for equilibration to occur. If we substitute our cloud parameters into their equation (4) and recalculate the conversion rate C, we find that the larger cloud particles produce a conversion rate of order 10^{12}, which is two orders of magnitude greater than the value obtained by Massie & Hunten. Thus, to produce roughly the same degree of equilibration given the faster rate of conversion, the effective eddy coefficient must be of order 10^6 cm^2 s^{-1}.

The fact that complete equilibration does not always occur may mean that the conversion process is less efficient than estimated by Massie & Hunten (1982) or that dynamical processes may come into play on time scales shorter than the equilibration time. In this discussion we have assumed, as did Massie & Hunten, that the product of the fraction of the active sites and the fraction of sites visited by an H_2 molecule when colliding with an aerosol particle is of order 10^{-4}. Should aspects of the surface chemistry result in lower quantum yields (i.e., less efficient conversion), the results presented above would have to be rescaled. Nevertheless, the larger NH_3 cloud particles allow for relatively fast conversion relative to dynamic mixing with a much lower product of these fractions. Additional experimental work is required to understand the surface chemistry in greater detail.

Chemical kinetic arguments related to the observed abundance of CO suggest that the eddy diffusion coefficient is of order 10^8 cm^2 s^{-1} in the deep troposphere (Prinn & Barshay 1977). Further, photochemical models suggest that the eddy coefficient at the 0.1 bar level is of order 10^3 cm^2 s^{-1} (Strobel & Yung 1979). Unfortunately, beyond these limiting values, the profile of the eddy coefficient is not well constrained in the Jovian atmosphere.

Since the rate of conversion depends on both particle size (surface area) and cloud optical depth, and since particle size changes little between belts and zones, optical depth variations between belts and zones are mainly responsible for the belt-zone variations observed in the cloud top para fraction. The optical depth dependence of the conversion rate results in a conversion rate that is about a factor of 5 larger in the NTrZ than in the NEB hot spots. This also accounts for the larger degree of equilibration observed in the colder NEB ensemble where the optical depth of the NH_3 cloud is 0.64 versus the 0.27 found in the NEB hot spots.

However, differences in the strength of the eddy diffusion coefficient (i.e., vertical mixing) seem to be responsible for the belt-zone variations in the height-dependent para-hydrogen profile. In both the cold NEB and EqZ ensembles, the retrieved NH_3 cloud optical depth is of order 0.6; nevertheless there are

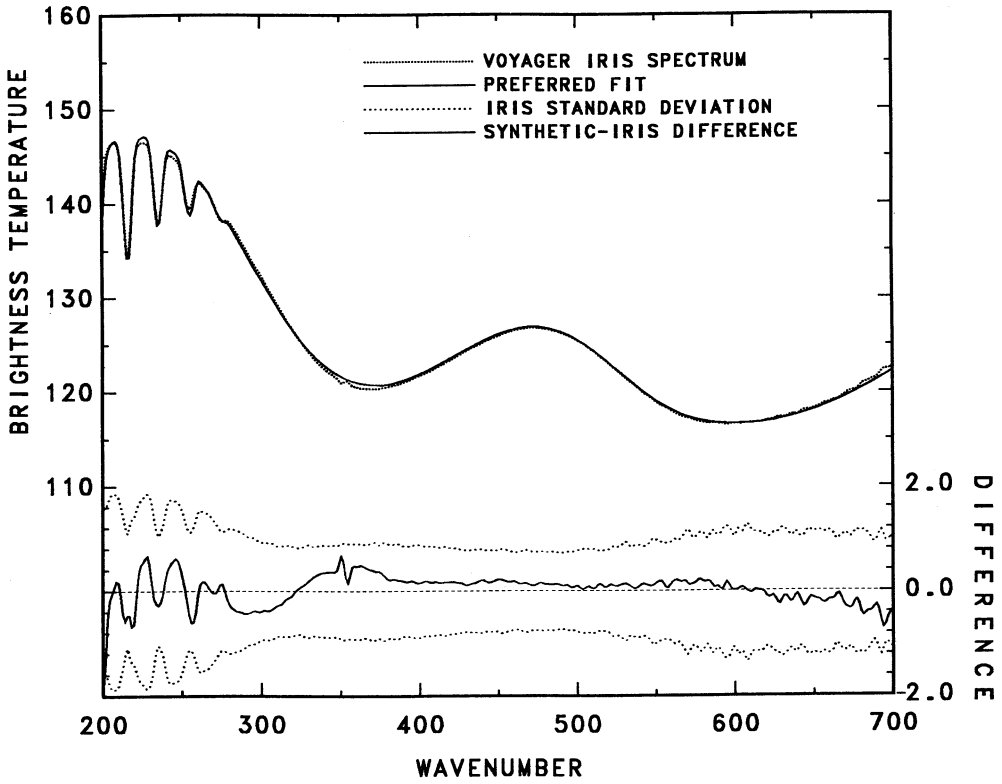

FIG. 10.—Comparison of our best-fit synthetic spectrum calculated with the height-dependent para-fraction profile with $P_L = 0.55$ bar, $P_U = 0.2$ bar, and a cloud top "equilibrated" para fraction $f_e = 0.32$ (*solid line*) and the average cold NEB spectrum (*dotted line*). The difference between the observed and synthetic spectra is shown in the lower portion of the figure (*solid line*) along with the standard deviation of the individual IRIS spectra comprising the ensemble (*dotted lines*).

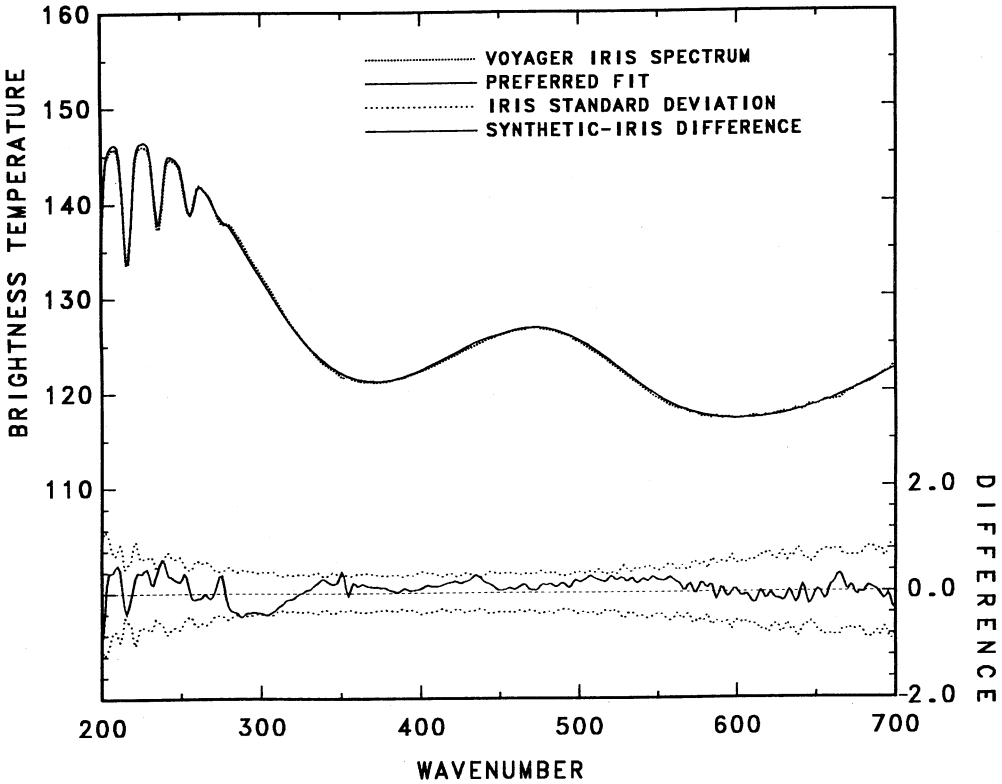

FIG. 11.—Comparison of our best-fit synthetic spectrum calculated with the height-dependent para-fraction profile with $P_L = 0.4$ bar, $P_U = 0.2$ bar, and a cloud top "equilibrated" para fraction $f_e = 0.33$ (*solid line*) and the average IRIS EqZ spectrum (*dotted line*). The difference between the observed and synthetic spectra is shown in the lower portion of the figure (*solid line*) along with the standard deviation of the individual IRIS spectra comprising the ensemble (*dotted lines*).

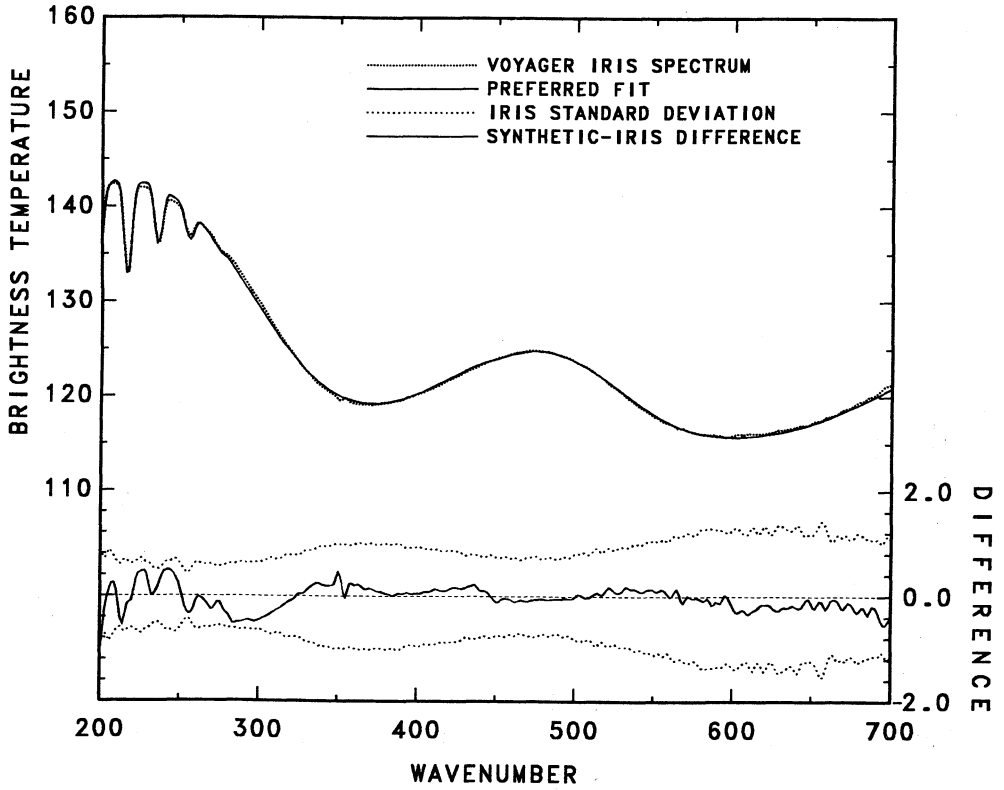

FIG. 12.—Comparison of our best-fit synthetic spectrum calculated with a height-dependent para-fraction profile with $P_L = 0.4$ bar, $P_U = 0.2$ bar, and a cloud top equilibrated para fraction $f_p = 0.35$ (*solid line*) and the average NTrZ spectrum (*dotted line*). The difference between the observed and synthetic spectra is shown in the lower portion of the figure (*solid line*) along with the standard deviation of the individual IRIS spectra comprising the ensemble (*dotted lines*).

distinct differences in the location of the para-hydrogen gradient that may be explained by the dynamic differences between these regions. In the cold NEB ensemble the inflection point P_L is located at 0.55 bar, whereas it occurs at 0.4 bar in the EqZ. The spectra comprising this cold NEB ensemble are located in the updraft (or stronger mixing) phase of wave motions within the NEB, while hot spots are found in the corresponding downdraft phase of the wave. We identify the updraft with larger (relative to the mean for each latitude band) NH_3 and H_2O relative humidities, larger PH_3 abundances above the 1 bar level, lower temperatures, and larger cloud optical depths. On the other hand, the downdraft (or weaker mixing) phase is characterized by reduced relative humidities, higher temperatures, lower PH_3 abundances above the 1 bar, and lower cloud optical depths (Carlson et al. 1992b, henceforth CLR92b). In all regions the updraft phase of the wave is associated with increased para fractions within the NH_3 cloud, which requires an increased conversion rate to offset mixing of lower para fraction parcels from below. Despite the larger para fractions overall, the changes in the para-hydrogen profile near cloud base in the EqZ and NTrZ/STrZ are consistent with dynamics being predominant. The stronger mixing results in lower para fractions advected from deeper to higher levels, hence the shift in the location of the lower inflection point P_L to 0.4 bar. The key case is that the changes in the cold NEB ensemble are not consistent with a purely dynamical interpretation. To increase the para fraction near the cloud base (i.e., shift the inflection point P_L to higher pressure), the wave updraft and mean downdraft would have to sum to a downdraft which conflicts with the increase in the NH_3 cloud optical depth. Rather, if the wave updraft and mean downdraft sum to a weak updraft sufficient to thicken the NH_3 cloud, but weaker than the updrafts in zones, then the increased para fraction near the cloud base can readily be explained, using the Massie & Hunten model, by enhanced conversion of ortho-hydrogen on the more numerous cloud particles in the presence of weak mixing.

Therefore, we conclude that ortho-para conversion is catalyzed by the presence of NH_3 cloud particles. Since UV solar photons are required to create an active surface site on the particle surface, equilibration does not occur on the surfaces of the deeper NH_4SH cloud particles.

Based on the model input parameters used by Massie & Hunten (1982), we conclude that the eddy coefficient is of order 10^6 cm^2 s^{-1} at the 0.5 bar level in belts and at the 0.4 bar level in zones (i.e., zones are upwelling regions). Our key conclusion is that, although ortho-para conversion is occurring in the NH_3 cloud, its rate is only slightly larger than the mixing rate at these levels. In general, mixing dominates in the region 0.4–0.5 bar, near the cloud base, whereas catalytic conversion dominates near cloud top, 0.2 bar. This strongly suggests that the NH_3 cloud is located in a region where the mixing rate decreases with altitude, which is also consistent with the small cloud optical depths and particle-to-gas scale height ratios.

The apparent transition from larger to smaller mixing rates that occurs at about the 0.5 bar level in belts and the 0.4 bar level in zones may indicate the top of the convectively mixed portion of Jupiter's troposphere. Such a transition at this level

is consistent with a rough equality of the radiative time constant and the estimated mixing required to move Jupiter's interior heat to higher altitudes (cf. Conrath & Gierasch 1984).

If convective transport of internal heat ceases near cloud base, it also suggests that the NH_3 cloud may affect the radiation of this energy to space. Moreover, the low optical depths of the NH_3 clouds suggest that significant amounts of sunlight are absorbed below NH_3 cloud level. Such an arrangement of solar heating and thermal cooling is similar to that in Earth's atmosphere, making it possible that cloud-radiation-dynamical interactions play a role in determining both the static stability and the nature of the circulation of the troposphere down to at least the 2 bar level. The large-scale correlation of changes in all of the clouds, including the water cloud, that we find (CLR92b) suggests that this circulation extends to water cloud levels near 5 bar.

While our para retrievals are too localized to constitute zonally averaged para fractions, our results are in conflict with the global picture presented in Conrath & Gierasch (1984, henceforth CG) and Gierasch et al. (1986, henceforth GCM). Their values of para fraction, which they estimate to be centered at 0.3 bar, have a minimum near the equator and increase monotonically toward the poles. The larger para fractions poleward of 35° latitude that they find might result from the effects of the changing emission angle with latitude interacting with the vertical para-hydrogen gradient not explicitly accounted for in their analysis. For the IRIS data near 60° latitude the cosine of the emission angle is roughly 0.6. This shifts the location of the peak emission level from 0.3 bar (near-nadir) to 0.2 bar. To investigate this possibility we used the IRIS mapping sequence observations to define an average spectral ensemble for the latitude region 40° to 60° N. Our best-fit para-hydrogen profile is specified by $P_L = 0.5$ bar, $P_U = 0.2$ bar, and $f_p = 0.33$. This f_p value is in excellent agreement with the high-latitude values reported by CG and GCM; however, they ascribed this value to the 0.3 bar level. Further, we note that for the EqZ and NTrZ, where our spectral ensembles are more representative of the zonal mean, our results are also consistent with those of CG and GCM. Since we have modeled the height dependence of the para-hydrogen profile by assuming that the gradient is linear, the value of f_p at 0.3 bar in the EqZ and NTrZ is simply the average of the upper and lower para fractions, that is, 0.29 and 0.3, respectively. Thus, it appears that the latitudinal gradient reported by CG and GCM is merely an artifact of the changing pressure level observed as emision angle changes in the presence of a para-hydrogen gradient.

In addition to reporting a para fraction, GCM also reported a para-hydrogen gradient df_p/dz^* where $z^* = \ln(P_0/P)$. Our profile can be converted to a gradient. We find that for NEB hot spots our value of df_p/dz^* is 0.07, which is in good agreement with the value 0.06 retrieved by GCM in the NEB. However, we find that df_p/dz^* is 0.12 in the EqZ and 0.14 in the NTrZ. These values are much larger than the near zero values reported by GCM. This may seem surprising given the good agreement between our comparisons of the retieved para fractions at the 0.3 bar level. We can however, reconcile this disagreement. While GCM use the variation in absorption strength between the $S(0)$ line center and edge to infer the para-hydrogen gradient, they neglect NH_3 cloud extinction. Since NH_3 cloud extinction provides significant absorption in the wing of the $S(0)$ line, they must add additional absorption to their model in order to reproduce the IRIS measurements. But since they do not include NH_3 cloud extinction, the only opacity source that they can add is additional para-hydrogen opacity. Thus they are led to infer an apparently higher para fraction in the wing of the $S(0)$ line than we obtain, which results in their near-zero gradient.

CG concluded that catalysis of ortho-para equilibration does not occur on NH_3 cloud particles based on the apparent lack of correlation between the latitudinal dependence of cloud indicators (they used visible albedo and 5 μm brightness temperature). Similarly GCM found no correlation between f_p and their cloud indicators (i.e., orange and blue reflectivities and 5 μm brightness temperatures). Given the low optical depths that we have retrieved for the NH_3 cloud ($\tau \leq 1$), variations in the albedo, as well as the visible reflectivities, are controlled by the deeper cloud structure (CLR92b). The 5 μm brightness temperatures are also controlled by the deep cloud structure (Marten et al. 1981; Bézard, Baluteau, & Marten 1983; CLR92a, b). Interestingly GCM reached the same conclusion. They used the orange relectivities to obtain an optical depth profile which they show in their Figure 9. They noted that the latitudinal dependence of the orange optical depths is remarkably similar in shape to that retrieved from their 5 μm inversion, but about a factor of 2 larger. From this they concluded that the same cloud particles are responsible for both the 5 μm and orange (0.585 μm), and that in both cases it is optical depth variations that cause the observed brightness variations. Further, we note good agreement between the orange optical depths retrieved by GCM and the total column cloud ($NH_3 + NH_4SH + H_2O$) optical depths that we retrieve (cf. CLR92a, b).

Thus, we conclude that CG and GCM did not find any correlation between para fraction and the NH_3 cloud primarily because they did not explicitly look for that correlation. Further, they misinterpreted their results because they did not explicitly correct for emission angle variability or the presence of a para-hydrogen gradient. Further, our results show that the CG conclusion of gradual equilibration from depth cannot be correct since para fractions in excess of 0.26 at pressures greater than 0.5 bar in belts and 0.4 bar in zones are inconsistent with the IRIS observations. Our results show a strong correlation between the location and magnitude of the para-hydrogen gradient and the location and optical depth of the NH_3 cloud (cf. Fig. 9) confirming the Massie & Hunten model.

We thank R. Hanel and the *Voyager* IRIS team for designing such a capable instrument and obtaining one of the finest planetary data sets. We thank A. D. Del Genio, L. D.. Travis, M. Allison, and Q. Ma for many helpful discussions. We would like to acknowledge the support of the Planetary Atmospheres Discipline, NASA Office of Space Science and Applications.

REFERENCES

Bachet, G., Cohen, E. R., Dore, P., & Birnbaum, G. 1983, Canadian J. Phys., 61, 591
Bézard, B., Baluleau, J. P., & Marten, A. 1983, Icarus, 54, 434
Birnbaum, G., & Cohen, E. R. 1976, Canadian J. Phys., 54, 593
Bjoraker, G. L., Larson, H. P., & Kunde, V. G. 1986, ApJ, 311, 1058
Carlson, B. E., Lacis, A. A., & Rossow, W. B. 1992a, J. Geophys. Res., submitted (CLR92a)
———. 1992b, J. Geophys. Res., submitted (CLR92b)
———. 1992, ApJ, 388, 648
Carlson, B. E., Prather, M. J., & Rossow, W. B. 1987, ApJ, 322, 559

Coffeen, D. L. 1974, J. Geophys. Res., 79, 3645
Conrath, B. J., & Gierasch, P. J. 1983, Nature, 306, 571
———. 1984, Icarus, 57, 184 (CG)
Del Genio, A. D., & McGrattan, K. B. 1990, Icarus, 84, 29
Dore, P., Nencini, L., & Birnbaum, G. 1983, J. Quant. Spectrosc. Radiat. Transf., 30, 245
Drayson, S. R. 1975, J. Quant. Spectrosc. Radiat. Transf., 16, 611
Gautier, D., Conrath, B., Flasar, M., Hanel, R., Kunde, V., Chedin, A., & Scott, N. 1981, J. Geophys. Res., 86, 8713
Gierasch, P. J., Conrath, B. J., Magalhães, J. A. 1986, Icarus, 67, 456 (GCM)
Hanel, R., et al. 1979a, Science, 204, 972
———. 1979b, Science, 206, 952
Hansen, J. E., & Travis, L. D. 1974, Space Sci. Rev., 16, 527
Husson, N., Goldman, A., & Orton, G. 1982, J. Quant. Spectrosc. Radiat. Transf., 27, 501
Kunde, V., et al. 1982, ApJ, 263, 443
Kunde, V. G., & Maguire, W. C. 1974, J. Quant. Spectrosc. Radiat. Transf., 14, 803
Marten, A., et al. 1981, Icarus, 46, 233
Martonchik, J. V., Orton, G. S., & Appleby, J. F. 1984, Appl. Opt., 23, 541
Massie, S. T., & Hunten, D. M. 1982, Icarus, 49, 213
Oinas, V. 1983, J. Quant. Spectrosc. Radiat. Transf., 29, 407
Pierluissi, J. H., Vanderwood, P. C., & Gomez, R. B. 1977, J. Quant. Spectrosc. Radiat. Transf., 18, 555
Prinn, R. G., & Barshay, S. S. 1977, Science, 198, 1031
Sassen, K., Grund, C. J., Spinhirne, J. D., Hardesty, M. M., & Alvarez, J. M. 1990, Month. Weather Rev., 118, 2402
Scott, N. A. 1974, J. Quant. Spectrosc. Radiat. Transf., 14, 691
Smith, W. H. 1978, Icarus, 33, 210
Strobel, D. F., & Yung, Y. 1979, Icarus, 37, 256